Design of a Magnetically-Geared Actuator for Extremely Cold and Dusty Space Environments

Justin J. Scheidler
NASA Glenn Research Center
Cleveland, USA
justin.j.scheidler@nasa.gov

Aaron D. Anderson
NASA Glenn Research Center
Cleveland, USA
aaron.d.anderson-1@nasa.gov

Thomas F. Tallerico
NASA Glenn Research Center
Cleveland, USA
thomas.tallerico@nasa.gov

Peter A. Hoge
HX5, LLC
Brook Park, USA
peter.a.hoge@nasa.gov

George R. Harpster
HX5, LLC
Brook Park, USA
george.r.harpster@nasa.gov

Kyle R. Whitling
HX5, LLC
Brook Park, USA
kyle.r.whitling@nasa.gov

Jesse Hawk
HX5, LLC
Brook Park, USA
jesse.hawk@nasa.gov

Malcolm Robbie
HX5, LLC
Brook Park, USA
malcolm.g.robbie@nasa.gov

***Abstract*— This paper presents the completed design of a rotational actuator composed of a concentric magnetically-geared motor and cycloidal magnetic gear for operation in dusty, vacuum environments where the actuator's temperature will vary between -249 C (24 K) to +101 C (374 K), e.g., the lunar surface. The requirements of the actuator are summarized, followed by a presentation of the electromagnetic, bearing, thermal, and structural designs. The predicted performance of the actuator over the full operating temperature regime and for a range of air gap sizes is presented.**

Keywords—magnetically-geared motors, space mechanisms,

I. Introduction

Conducting science in permanently shadowed and polar regions of the Moon, on bodies that may possess life, and in orbiting platforms that experience prolonged deep cold when shadowed requires rotational actuators that can operate reliably in extreme cold. Heating the actuators and using conventional grease-lubricated gears and bearings adds complexity and mass and will be impractical or highly undesirable because surface missions on these bodies are expected to be severely power constrained [1]. Solid lubricants are a mature technology that allow mechanisms to operate without heating below -60 °C but at a significant cost to a mechanism's life and the load capacity of its lubricated contacts. The penalties with solid lubricants may be manageable in bearings but are usually severe in gears due to the much higher amount of sliding in a gear tooth contact. Magnetic gearing eliminates the gear lubrication challenge, making it feasible to achieve long life.

NASA's Motors for Dusty & Extremely Cold Environments (MDECE) Project is developing a magnetically-geared actuator for long duration operation on the Moon where there is no atmosphere, surface temperatures reach 30 K (-243 °C), and the very fine lunar soil creates a dust exposure hazard. The objectives of this project, detailed in [1], are to be operable without supplementary heating when the surface temperature is 108 K (-165 °C) (threshold) to ≤ 30 K (goal), have a total efficiency of 60% (threshold) to ≥ 80% (goal) under continuous operation, and achieve a life in a dust-free environment of 6,000 (threshold) to ≥ 50,000 (goal) output revolutions. Initial design studies and a proof-of-concept actuator are presented in [2][3]. This paper presents the detailed design of the final actuator.

This work was supported by the Motors for Dusty & Extremely Cold Environments (MDECE) Project within NASA's Game Changing Development Program and the Space Technology Mission Directorate.

Notice for Copyrighted Information: This manuscript is a joint work of employees of the National Aeronautics and Space Administration and employees of HX5, LLC under Contract No. 80GRC020D0003 with the National Aeronautics and Space Administration. The United States Government may prepare derivative works, publish, or reproduce this manuscript and allow others to do so. Any publisher accepting this manuscript for publication acknowledges that the United States Government retains a non-exclusive, irrevocable, worldwide license to prepare derivative works, publish, or reproduce the published form of this manuscript, or allow others to do so, for United States government purposes.

II. Actuator Overview

The design specification for the actuator's output is a continuous rating of 105 Nm at 2 rpm and a peak rating of 208 Nm at 1.5 rpm for at least 60 s. Fig. 1 depicts a model of the actuator and its key subsystems and components. Following a quantitative comparison of multiple actuator configurations, two stages of magnetic gearing were chosen for the actuator – a concentric magnetically-geared motor with a gear ratio of 13.5 connected to a cycloidal magnetic gear with a gear ratio of 43. A commercial-off-the-shelf resolver was included in the design to realize closed loop control of the actuator's motor in testing, but it may not be needed in a flight variant of the actuator. A dust seal was incorporated around the actuator's output shaft to minimize lunar regolith (soil) ingestion.

III. Detailed Design

This section presents a summary of the core elements of the actuator's design.

A. Electromagnetic Design

Two design codes were developed to separately configure, size, and optimize the cycloidal magnetic gear and magnetically-geared motor. The sequence of calculations in the motor code starts with 2D electromagnetic finite element simulations to determine the torque and magnetic forces per unit stack length (including the predicted impact of 3D effects on electromagnetic performance) [4]. The required axial length of the component is calculated and analytical mechanical design equations are used to size structures and shafts. Bearings with an optimal combination of life and loss are selected based on the analysis

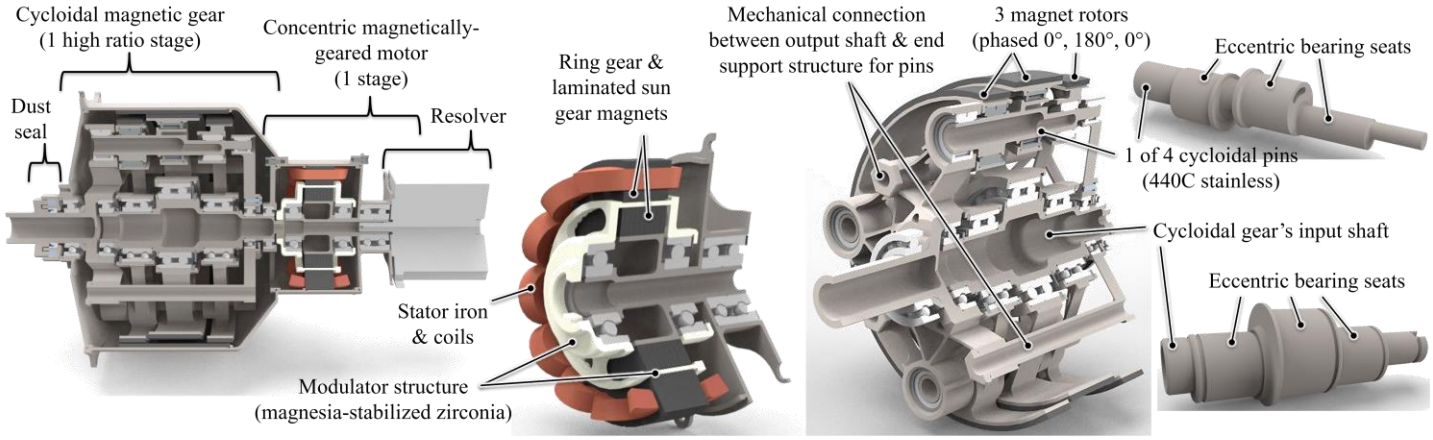

Fig. 1. Cryogenic-operable magnetically-geared actuator: (left) assembled actuator with key subassemblies labeled, (center) concentric magnetically-geared motor, and (right) cycloidal magnetic gear. All magnets are made of Sm2Co17, the stator iron and modulator pole pieces are composed of Fe49.5Co48.5V1.9, and all structures are made of Ti-6Al-4V unless otherwise noted.

described in Section III.B. A thermal finite element model of the motor's stator and attached ring gear magnets is used to ensure a valid thermal design. This sequence is iterated within an open source genetic optimization algorithm [5] to minimize the mass and continuous losses of the motor by altering the motor's geometry and gear ratio.

The design code for the cycloidal magnetic gear follows the same format except that (a) no thermal analysis is conducted and (b) selection of bearings is done before the mechanical design because iterations are required to determine the magnetic stack length needed to achieve the desired peak torque after all losses are accounted for.

Sizing of the geared motor depends on the gear ratio and efficiency of the cycloidal magnetic gear. Thus, the magnetic gear was first optimized for fixed gear ratios within a range determined by the preliminary design and then the gear's mass and efficiency as a function of its gear ratio were input into the motor optimization to produce an optimum solution.

The actuator was designed with nominal air gaps of 0.25 mm. An initial stack-up analysis of part tolerances suggested that the air gaps could have a tolerance of ±0.15 mm. Thus, the gear and motor were sized magnetically for 0.4 mm air gaps. The gear was designed with a 15% margin on peak torque. The motor was designed with a 20% margin on torque.

The cycloidal magnetic gear was designed with three wobble rotors [15] because that was predicted to provide a 1.3 kg reduction in the actuator's mass relative to one rotor, due to a significant reduction in bearing loads and the elimination of a counterbalance. The optimal number of cycloidal pins was found to be four. Fewer pins led to higher bearing loads and thus reduced efficiency and greater mass. More pins added complexity with no predicted improvement in efficiency or mass. Transferring the magnetic forces to the pins and output shaft through needle bearings was found to provide significant mass and efficiency improvement over transfer through sliding pin-to-wobble rotor contact, due to reduced bearing loads as explained in [2].

The performance of the optimized motor was evaluated for both concentrated and distributed windings and both block commutation and field oriented control. Concentrated windings were selected due to its simplicity and calculated higher efficiency. Field oriented control was selected for reduced resistive loss and torque ripple. The predicted magnetic losses and efficiency at different temperatures is summarized in Table 1.

TABLE I. MAGNETIC LOSSES AND MAGNETIC EFFICIENCY OF THE GEARED MOTOR UNDER CONTINUOUS OPERATION.

Loss [W]		**Temperature [K]**				
		50	***150***	***250***	***350***	***450***
Eddy currents	Sun magnets	0.10	0.09	0.08	0.07	0.06
	Modulator	0.15	0.14	0.14	0.14	0.13
	Ring magnets	0.07	0.07	0.06	0.05	0.05
	Stator iron	0.77	0.77	0.76	0.74	0.71
Winding losses	Proximity	0.86	0.05	0.03	0.02	0.01
	Ohmic	0.06	0.84	1.65	2.54	3.53
Efficiency, %		91.7	92.0	89.2	86.3	83.2

The electromagnetic simulations were used to calculate the magnetic force on each magnet and pole piece for input to the bearing analysis and structural finite element analysis (FEA).

B. Bearing Design

Cylindrical roller bearings were used between the cycloidal pins and mating rotors. For all other locations, super precision angular contact ball bearings were used. The bearings were optimized assuming 440C stainless steel races, Si_3N_4 balls, 52100 steel rollers, MoS_2 sputtered on raceways and rolling elements, and PGM-HT cages.

For each of the 15 locations of bearings in the actuator, the power loss and life of a whole catalog of commercial bearings was evaluated. The load distribution on each rolling element was iteratively calculated as a function of time for an applied axial and radial load per [6]. At each raceway-rolling element contact, the contact area and contact stress [6] and the MoS_2 film life

were then calculated at each time. The film life L in revolutions was estimated as

$$L = 2.7e20\ \sigma^{-4.53}, \quad (1)$$

where σ is the mean Hertzian contact stress in units of MPa, based on a limited dataset in [8]. The sliding friction forces, moments, and power loss were then quantified per [6] using a coefficient of sliding friction μ at each contact estimated as

$$\mu = \tau A / F, \quad (1)$$

where A is the contact area, F is the contact force, and τ is the shear strength of the lubricant (24.8 MPa per [7]) [8]. This coefficient of friction gave values around 0.03 and is valid early in the bearing's life when the MoS_2 film dictates the lubrication. Later in the life, the cages dictate lubrication by transferring a film to the raceways. In this regime, a constant coefficient of friction of 0.25 was used as suggested in [8].

The axial load was taken as the spring preload on each bearing, and the radial load was based on magnetic forces. During electromagnetic optimization, the preload was fixed and the radial loads were calculated analytically to reduce the computation time. For final bearing optimization after the magnetic design was finalized, the radial load was extracted from the structural FEA (except for the needle bearings in the three wobble rotors, for which the radial load was analytically calculated and time varying) and the preload class of each ball bearing was optimized. The final bearing optimization accounted for the temperature dependence of material properties, changes in internal clearance due to the possible fits between the bearing and its mating hardware and differential thermal expansion [9][6], and the predicted variation in bearing preload due to thermal expansion and tolerances on the preload spring's spring rate and working height (due to tolerances on hardware in the preload force load path).

Fig. 2 shows the results of optimizing a heavily loaded bearing in the actuator. In this case, several lightweight, smaller bearings meet the project's life threshold but only heavy, larger bearings reach the life goal. The optimization was constrained to allow room temperature assembly (clearance fit to either the housing or shaft at room temperature). The bearing performance

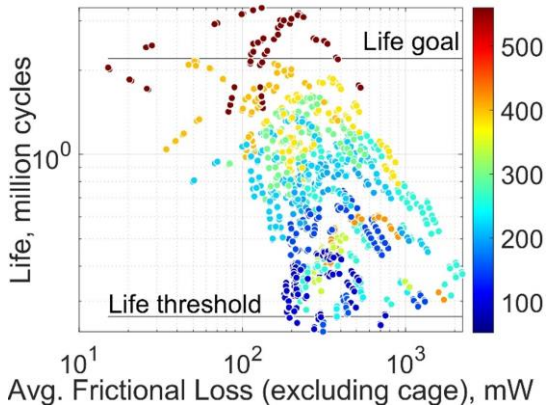

Fig. 2. Optimization results for the mass (units of g), life, and frictional loss of one heavily-loaded bearing.

was optimized for continuous operation and a 30 K lunar surface, for which the predicted steady state temperature of the bearing's was about 120 to 150 K.

The stiffness matrix of each bearing under the aforementioned axial and radial loads was calculated and utilized in the structural FEA.

C. Thermal Design

The steady state and transient thermal response of the actuator was simulated using a model that combines finite difference primitives and finite elements. The geometry, shown in Fig. 3, was imported from CAD and reduced using common simplifications (e.g., combine magnets from one array into a single solid, ignore fasteners & small features). The actuator was not developed for a specific mission. Thus, it was modeled as floating ~0.5 m from the lunar surface with only radiative heat transfer to the environment (i.e., no conduction to other hardware of a lander/rover). The model included contact conductances between mating parts based on contact pressures from structural FEA and bearing fits. The temperature-dependent thermal conductance of the solid lubricated bearings was calculated according to [10]. A 20% reduction in the conductance was applied to account for MoS2 lubricant film on balls and races per [11]. The temperature dependence of heat loads (both magnetic and bearing friction) and the thermal conductivity and specific heat of materials were also accounted for. A constant heat load of 25 mW per contact seal in the dust seal assembly was applied. Optical properties (emissivity ε and absorptivity α) for each material were either found in the literature or measured using a handheld emissometer.

The external surface finish or coating of the housing is an important design choice for radiatively cooled actuators [1]. For grease lubricated actuators that must be heated to about -60 °C or higher, there is a tradeoff between a finish/coating that keeps the actuator warmer in cold, shadowed environments (high α / ε) and one that keeps the actuator cooler in hot, sun lit environments (low α / ε). Since the MDECE actuator is operable at cryogenic temperatures, it eliminates this tradeoff and allows the finish/coating to be optimized for the hot case only, which

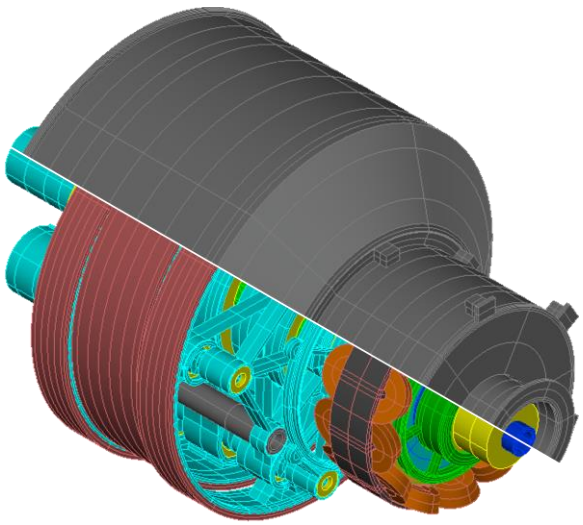

Fig. 3. Geometry and discretization of the thermal model with the housing and outer cycloidal magnets partially hidden.

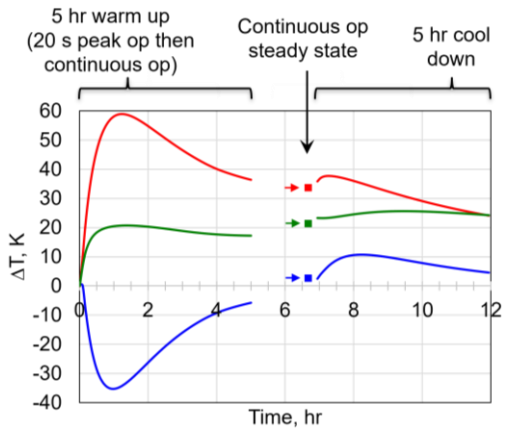

Fig. 4. Predicted temperature gradient across the air gaps during transient warm up, steady state continuous operation, and transient cool down; the response at 1.1 hr was used as a worst case for structural analysis of the change in air gap.

improves the actuator's operating temperature range and enables it to operate closer to the Moon's equator and survive at the equator in the sun. Accordingly, two surface finish or coating options were evaluated – a 'type 1' anodize of the titanium housing (commercially available, no temperature limitation; $\alpha / \varepsilon = 0.697$) and Solar White [12] (being commercialized, low temperature limit unknown; $\alpha / \varepsilon = 0.038$).

The model was solved for each operating and survival environment defined in [2] and for transient warm up and cool down cases. The thermal margin for each material was calculated by comparing predicted temperature limits to material limits. The maximum temperature of actuator components was predicted to be 86-98 °C for the anodized coating and 56-101 °C for the Solar White coating. Consequently, hot thermal margins were >140 °C except for the cryogenic-rated epoxy (34 °C margin, which is greater than the 21 °C margin required by [13]). The minimum survival and operating temperature for all materials were -258 °C and -249 °C, respectively. Cold thermal margins were positive except for the meta-aramid polymer used in the dust seal, although that is thought to be a result of limited cryogenic material data because two similar polymers are rated to 4 K (-269 °C).

A key output of the thermal model is the predicted temperature gradient across each bearing and air gap. This was calculated from transient and steady state responses as a function of temperature and then utilized to predict the temperature-dependent bearing performance. The worst-case condition for thermal-induced changes in the air gaps was also identified from these outputs, as depicted in Fig. 4. The temperature distribution at this time was applied in the structural FEA for the 'worst-case cold' analysis.

D. Mechanical Design

The mechanical design of the actuator was based on the bearing design, a tolerance stack-up analysis, a manufacturability assessment, and a structural finite element model. Fig. 5 depicts the geometry and mesh of the finite element model, which included the full complexity of the CAD model except that bearings were modeled as a stiffness matrix

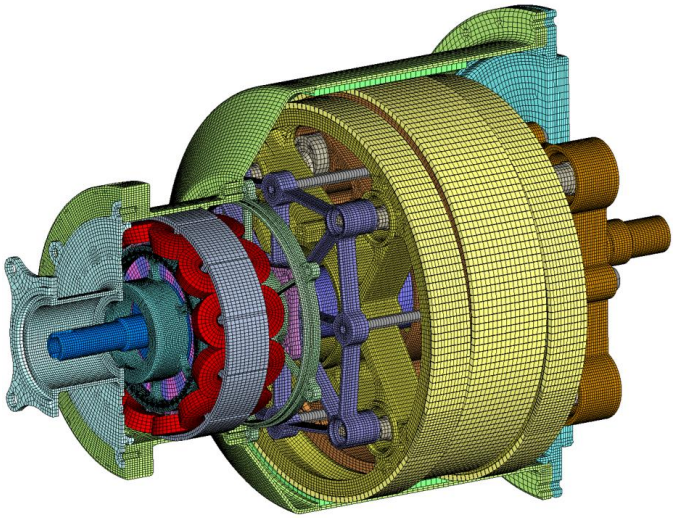

Fig. 5. Geometry and discretization of the structural model of the as-built actuator with the housing and outer cycloidal magnets partially hidden.

using a spring element rather than solid geometry. Mechanical contact without slip was used to model interfaces that are not bolt preloaded or glued. Bonded joints were used for all epoxied interfaces except for the magnet's epoxy bonds. Preliminary results showed excessive stress at the interfaces between magnets, other magnets, and the structure on which they are adhered. Thus, the epoxy layer at these interfaces was explicitly modeled to increase fidelity. Translational constraints were applied to the housing's mounting bolt pattern via bolt stiffness elements. The input end of the geared motor's sun rotor and the output end of the actuator's output shaft were torsionally fixed. Radial and torsional magnetic forces were applied to the magnets and modulator pole pieces. The cycloidal gear was sized for the largest anticipated air gaps, as noted in Section III.A, but the magnetic forces were determined for the smallest anticipated air gaps (0.1 mm) to yield the largest possible forces. Centrifugal loads were applied to the sun rotor and modulator but not the rotors in the cycloidal gear due to their low speed (86 rpm). Bearing preload forces for the optimized bearings were included. Thermal loads were included by applying the thermal model's temperature predictions and temperature-dependent thermal expansion coefficients. To be conservative, room temperature material strengths were used in quantifying stress margins. The factors of safety used for metallic, adhesive, and ceramic materials were taken from Tables 1, 2, and 3, respectively, in [14].

The structural FEA model was simulated for four cases: room temperature, start of cold operation (uniform temperature of -249 °C), worst-case cold operation, and worst-case hot operation. In each case, the peak torque condition was modeled because it yields the largest stresses. The radial deformation of components on each side of the air gap was extracted in each case to assess the change in air gap. The effect on air gaps in the geared motor was minimal due to the magnetic and centrifugal forces being relatively small and fairly symmetric. The effect in the cycloidal gear was more pronounced. Across all cases, the minimum air gap in the gear *increased* by 0.01 mm to 0.08 mm due to the orientation of the magnetic forces under peak torque.

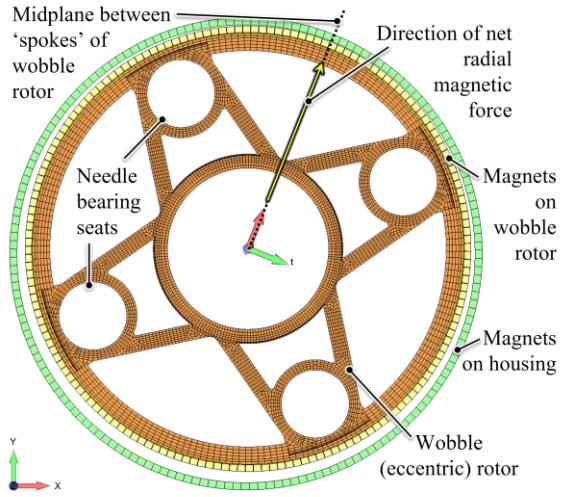

Fig. 6. Axial view of one wobble rotor in the cycloidal gear depicting the overall worst-case condition for reduction of the air gap due to structural deformation. Worst-case load (zero torque, when radial magnetic forces act in the direction of minimum air gap) and worst-case time (minimum gap aligned with rotor's most compliant direction).

The influence of temperature on the air gaps was found to be small.

In the cycloidal gear, the worst-case load for air gap deformation is at zero torque when the net magnetic forces act radially toward the position where the nominal gap is minimum. Fig. 6 shows the worst-case condition. At zero torque, the minimum air gap *reduced* by 0.06 mm, which is significant but does not eliminate the air gap under worst-case tolerance stack up. Wear of the bearings is not expected to impact the air gaps, because the MoS_2 lubricant films are only 1±0.5 µm thick and the bearings were sized for life based on the solid lubricant's life (MoS_2 film and lubricant transfer film from the cage). As a result, the contact stresses are limited to only about 10% to 40% of what a grease-lubricated bearing can tolerate. For example, the most heavily loaded bearing is predicted to have an L10 fatigue life (i.e., conventional bearing failure) that is 45 times the goal actuator life, whereas failure due to the solid lubricant is estimated to occur at 0.3 to 1.5 times the goal life.

Initially, the model indicated negative stress margins for the cold cases in one of the modulator's end caps and in the magnets and epoxy on the gear's wobble rotors. The end cap margin was made positive by switching the material from alumina to magnesia-stabilized zirconia. For the wobble rotor magnet and epoxy stresses, it was determined that the titanium rim of each wobble rotor was too compliant and was deformed into a noncircular shape. Stresses were reduced by stiffening the wobble rotors' rim and 'spokes', but the benefit plateaued as increased thickness led to more thermal stress between the rotors and magnets. A 48% reduction in the max principal stress in the magnets was achieved, yielding a healthy margin of 0.9. The predicted stress in the epoxy reduced by 41%, leaving a margin of –0.2. This negative margin was accepted because it only occurred in very small regions of epoxy between adjacent magnets and thus is unlikely to cause magnets to break free from rotors. The added stiffness to the wobble rotors also helped reduce the air gap deformation by 50% to the number reported above.

A modal analysis of the actuator was also completed using the structural FEA model, in part to determine if the bearing preload springs were too compliant. For this analysis, the mass of each bearing was included as lumped masses (55% lumped into the bearing's housing and 45% into its shaft). The excitation with highest frequency is the sun rotor's rotation (19 Hz), which can excite rotordynamic critical speeds up to 39 Hz. The lowest mode (axial oscillation of wobble rotors on the preload spring for the eccentric bearing) was found to be 51 Hz, which provides ample margin to 39 Hz. Further, the sun rotor's rotation is unlikely to be capable of exciting the mode. The next lowest mode was 66 Hz.

Splitting the cycloidal gear into three wobble (eccentric) rotors introduces practical challenges, as noted in [15]. Angular misalignment of magnets from one wobble rotor to another is one concern. This was addressed by including a shallow groove just wide enough for one magnet in the outer diameter of each wobble rotor. These grooves were aligned and used as a datum while match grinding bearing bores in the rotors. Three additional grooves spaced 90° apart were included in each rotor to limit the impact of the stacking the magnet width tolerance by re-establishing the circumferential position of every 43rd magnet. The position of the eccentric bearing seats on the cycloidal pins and cycloidal input shaft was also very tightly controlled to minimize misalignment.

Another concern with three wobble rotors is the stack up of manufacturing tolerances on the air gaps and the ability to assemble the cycloidal pins into the 3 wobble rotors, output shaft, and support rotor. A final stack up analysis predicted a tolerance band of ±0.09 mm on each air gap in the gear if a traditional manufacturing approach were used with very tight tolerances. However, a method was devised to match grind the bearing seats in the gear's rotors with only 2 fixture setups. This nearly eliminates several tolerances and was predicted to enable an air gap tolerance band of ±0.027 mm. The ability to assemble requires very tight tolerances, particularly on the cycloidal pins and cycloidal input shaft. To satisfy this concern and attempt to meet the tolerances specified by the manufacturer of the super precision ball bearings, a cylindricity tolerance of 2–5 µm was used on the eccentric bearing seats along with a position tolerance of 2–4 µm relative to the non-eccentric bearing seats. The predicted tolerance band of the air gaps in the motor was 0.04 mm and 0.06 mm.

IV. Predicted Performance

Table 2 shows the impact of the possible air gap variation (from the initial tolerance stack-up analysis) on the peak torque and specific torque of the actuator. The mass of the actuator without the resolver is summarized in Table 3. The total mass (4.55 kg) is very similar to the mass predicted by the design code (4.63 kg). The magnetic mass is 38% of the total. The resolver does add 0.75 kg, but a proof-of-concept actuator indicates that three Hall sensors embedded in the motor's stator iron can replace the resolver and provide sufficient sun rotor position feedback for motor control. The actuator's diameter, not including its mounting flange, is 153 mm and its length is 240 mm, and its envelope volume is 2,317 cm^3. In the design

TABLE II. CHANGE IN PEAK TORQUE AND SPECIFIC TORQUE OF THE AS-DESIGNED ACTUATOR WITH AIR GAP; THE PEAK TORQUE OF THE CYCLOIDAL MAGNETIC GEAR AND MAGNETICALLY-GEARED MOTOR INCLUDES A 5.5% AND 34.5% REDUCTION, RESPECTIVELY, FOR 3D EFFECTS.

Air gap [mm]	Magnetic gear		Geared motor			Actuator		
	Peak torque [Nm]	*Specific torque [Nm/kg]*	*Peak torque [Nm]*	*Specific torque [Nm/kg]*		*Peak torque [Nm]*	*Specific torque [Nm/kg]*	
				With resolver	*No resolver*		*With resolver*	*No resolver*
0.1	282.6	78.7	-	-	-	282.6	53.3	62.1
0.25	257.0	71.6	7.56	4.4	7.9	257.0	48.5	56.5
0.4	231.2	64.4	5.62	3.3	5.9	231.2	43.6	50.8

TABLE III. MASS BREAKDOWN OF THE AS-DESIGNED ACTUATOR (WITHOUT THE RESOLVER).

Component	Magnetic (stator) [kg]	Magnetic (other) [kg]	Structure [kg]	Bearings [kg]	Hardware / other [kg]	Total [kg]
Geared motor	0.31	0.30	0.20	0.14	0.01	0.96
Magnetic gear	n/a	1.11	1.78	0.59	0.11	3.59
Actuator	0.31	1.41	1.98	0.73	0.12	4.55

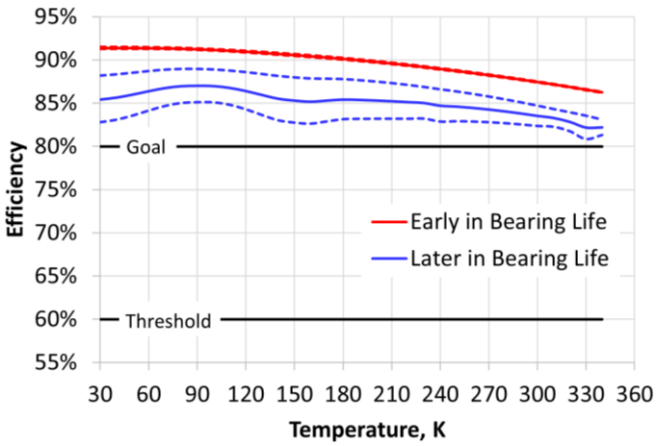

Fig. 7. Efficiency of the actuator versus operating temperature at its rated continuous output both early and later in bearing life; dashed lines correspond to a 99.7% confidence interval on the bearing losses, which results from uncertainty in the actual internal clearance in each bearing and the actual spring preload on each bearing.

environments, the actuator is predicted to operate at internal temperatures between –249 °C and +101 °C, although colder temperatures should have little impact. Fig. 5 presents the actuator's efficiency at its rated continuous output torque (105 Nm) over a wide operating temperature range. The efficiency is predicted to exceed the project's goal of 80% throughout the temperature range and life of the actuator. The predicted life, governed by the bearings, is 46,500 output revolutions.

V. CONCLUSIONS

This paper summarized the completed design of a magnetically-geared actuator for operation in extremely cold vacuum environments like the polar regions of the lunar surface. The actuator is predicted to operate at internal temperatures between –249 °C and +101 °C with an efficiency over 80% and a life that is useful for lunar applications. A lightweight magnetic design is enabled through the use of 0.25 mm air gaps. Achieving this air gap size is difficult due to the complexity of the cycloidal gear, but a solution was found that enables 0.25 mm air gaps with a -0.09 / +0.11 mm tolerance across all operating conditions, including structural deformation and the stack up of manufacturing tolerances. With the small air gaps enabling lightweight magnetics, the actuator's size and mass is largely driven by the sizing of the solid lubricated bearings based on a limited data set and the bearings' impact on the configuration of the cycloidal magnetic gear. Lifetime testing of the actuator will be informative for whether the bearings can be shrunk in future iterations.

REFERENCES

[1] J. Scheidler, E. Stalcup, and E. Montbach, "The impacts of heating actuators in extremely cold space environments," in Proc. IEEE Aerospace Conference, 2022.

[2] J. J. Scheidler et al., "Detailed design of a magnetically-geared actuator for use in extremely cold lunar environments," In Proc. IEEE Aerospace Conference, 2023.

[3] J. J. Scheidler et al., "Development and manufacture of a proof-of-concept magnetically-geared actuator for use in extremely cold lunar environments," In Proc. 20th European Space Mechanisms and Tribology Symposium. 2023.

[4] T. F. Tallerico, Z. A. Cameron, J. J. Scheidler, and H. Hasseeb, "Outer Stator Magnetically-Geared Motors for Electrified Urban Air Mobility Vehicles," In Proc. AIAA Propulsion and Energy Forum, 2020.

[5] S. D. Sudhoff, "Genetic optimization system engineering toolbox 2.6," 2013. [Online]. Available: https://engineering.purdue.edu/ECE/Research/Areas/PES/Software/genetic-optimization-toolbox-2.6

[6] T. A. Harris, Rolling Bearing Analysis, 2nd ed., Wiley, 1984.

[7] M. R. Vazirisereshk, A. Martini, D. A. Strubbe, and M. Z. Baykara, "Solid lubrication with MoS_2: a review," Lubricants, vol. 7, no. 7, 2019.

[8] European Space Tribology Laboratory, Space Tribology Handbook, 2023.

[9] NSK, Technical Report, CAT. No. E728h, 2024. [Online]. Available: https://www.nsk.com/site-search-result/?q=E728

[10] M. M. Yovanovich, "Thermal constriction resistance between contacting metallic paraboloids: Application to Instrument Bearings," in Proc. AIAA Progress in Astronautics and Aeronautics, Heat Transfer and Spacecraft Thermal Control, vol. 24, 1971.

[11] M. J. Anderson, "The thermal conductance of solid-lubricated bearings at cryogenic temperatures in vacuum." in Proc. 30th Aerospace Mechanisms Symposium, 1996.

[12] R. C. Youngquist, M. A. Nurge, W. L. Johnson, T. L. Gibson, and J. M. Surma, “Cryogenic Deep Space Thermal Control Coating,” J. Spacecr. Rockets, vol. 55, no. 3, 2018.

[13] Air Force Space Command, “Test requirements for launch, upper-stage and space vehicles,” Space and Missile Systems Center Standard SMC-S-016, 2014.

[14] National Aeronautics and Space Administration, “Structural Design and Test Factors of Safety for Spaceflight Hardware,” NASA-STD-5001, 2022.

[15] B. Praslicka et al., “Practical Analysis and Design of a 50:1 Cycloidal Magnetic Gear with Balanced Off-Axis Moments and a High Specific Torque for Lunar Robots,” In Proc. IEEE Int. Electr. Mach. Drives, 2021.